PAPER

Check for updates

Electrolyte additive strategy for uniform nucleation of Cu−Bi toward low-voltage self-powered dynamic windows†

Xi Wang,[a] Yiming Bai,*[ab] Fei Han,[a] Yichen Jiao,[a] Yuzhe Guan,[a] Jinjing Bai,[a] Fuzhi Wang,[a] Meicheng Li [ID] [a] and Guicheng Liu [ID] *[acd]

Reversible metal electrodeposition devices (RMEDs) powered by solar cells have shown promise in energy-saving buildings. However, the high driving voltage and unclear nucleation/growth mechanism of metal particles have hindered their application. Herein, we propose an electrolyte additive strategy to lower the driving voltage and develop an integrated RMED, where Cu−Bi RMED is driven by CsPbI$_2$Br solar cells. Results confirm that our integrated device can achieve a fast chromatic transition from transparent to black only under sunlight, displaying 62.42% optical contrast and outstanding performance durability. Studies on the dynamic nucleation mechanism reveal that the introduction of choline chloride (ChCl) in water can provide more theoretical nucleation sites (from 4.94 to 13.55 μm^{-2}) and facilitate an easier electrodeposition process, resulting in uniform/dense bimetallic films. Experimental results indicate that the ionic conductivity increases from 0.05 to 0.31 S m^{-1}, and the charge transfer resistance decreases from 3834 to 647 Ω cm^2 upon the introduction of ChCl, leading to fast nucleation and color-change at low driving voltage. Furthermore, CsPbI$_2$Br solar cells, with an open-circuit voltage of up to 1.32 V, guarantee smooth operation of the integrated device *via* Pb(Ac)$_2$ modification and L-phenylalanine (L-PAA) passivation. Hence, the application limitations of RMED might potentially be overcome by introducing appropriate electrolyte strategies.

1. Introduction

With the rapid development of urbanization, various modern buildings have sprung up, creating a modern and fashionable atmosphere in cities and becoming eye-catching landmarks, especially steel-and-glass skyscrapers. However, this growth has led to increased energy consumption for heating and cooling. Dynamic windows, which enable smart control of solar light and heat *via* voltage, can yield an average of 20% energy saving in buildings and improve employee happiness and productivity by up to 2% *via* reduced glare and lighting control. They are being extensively promoted as one of the solutions for decarbonizing buildings.[1,2]

Dynamic windows based on reversible metal electrodeposition devices (RMEDs) stand at the forefront of groundbreaking technology due to their fast switching speed, color neutrality, tunable transparency, and low cost.[3] However, their practical application still suffers from certain limitations.[4] The first involves the external power supply, which can trigger optical response lag due to cumbersome external wiring, hindering application.[5] The second relates to driving voltage, as operating at high voltage consumes more energy and may cause device performance deterioration.[6] To address the first issue, using solar cells (SCs) as a power source to drive RMEDs appears feasible if the output voltage of SCs is sufficiently high to support the electrochemical reduction and oxidation process. This integration can be achieved in a stand-alone device, effectively avoiding the optical response lag caused by cluttered device wiring.[7] Single-junction CsPbI$_2$Br-based solar cells, known for their potential high output voltage and impressive stability, have emerged as promising candidates for integrated photovoltachromic devices. Current research on CsPbI$_2$Br solar cells focuses on suppressing carrier recombination and enhancing the open-circuit voltage (V_{oc}).[8,9] For the latter, lowering the driving voltage of RMEDs is necessary for their commercial application as the values of driving voltage

[a] State Key Laboratory of Alternate Electrical Power System with Renewable Energy Sources, North China Electric Power University, Beijing 102206, China. E-mail: ymbai@ncepu.edu.cn; gcliu@ncepu.edu.cn; log67@163.com

[b] Key Laboratory of Semiconductor Materials Science, Beijing Key Laboratory of Low Dimensional Semiconductor Materials and Devices, Institute of Semiconductors, Chinese Academy of Sciences, Beijing 100083, China

[c] Fujian Provincial Key Laboratory of Eco-Industrial Green Technology, Wuyi University, Wuyishan, Fujian Province, 354300, China

[d] Key Laboratory of Power Station Energy Transfer Conversion and System of Ministry of Education, School of Energy Power and Mechanical Engineering, Beijing Laboratory of New Energy Storage Technology, North China Electric Power University, Beijing, 102206, China

This journal is © The Royal Society of Chemistry 2025

J. Mater. Chem. A, 2025, **13**, 10049–10059 | **10049**

dominate device transmittances through the oxidization of metal for window bleaching or the reduction of metal ions for window tinting.[10–12] Low voltage means achieving high optical contrast with reduced energy consumption. The driving voltage greatly depends on the electrolyte, which plays a crucial role in metal nucleation and growth.[13] Currently, the cationic selection of salts for the electrolytes includes Li^+, Cu^{2+}, Zn^{2+}, Ag^+, Al^{3+}, Pb^{2+}, and others.[14–16] The widely used solvents include aqueous and deep eutectic solvents (DESs).[17] Aqueous electrolytes have the advantages of high solubility for metal salts, high conductivity, and nontoxicity, but they are limited by the hydrogen evolution reaction and passivation effects caused by the formation of insoluble oxides or hydroxides on the electrode, which inhibits deposition of target metals.[18] DESs can avoid passivation effects and offer advantages, such as wide electrochemical windows and high solubility for metal salts, metal oxides, and hydroxides.[19] However, the current density for electrodeposition in DESs is relatively low at high-driving voltages compared to that of aqueous electrolytes.[20] Hence, there is an urgent need to develop an electrolyte that combines both aqueous and DESs for ideal RMEDs with low self-driving voltage.

In the last few years, significant progress has been made in RMED with low driving voltages. Wang Ting *et al.* proposed an RMED system using a $ZnSO_4/CuCl_2$ solution as the electrolyte and Prussian blue as the counter electrode.[21] In this system, the optical contrast of the device reached as high as 60% by applying a voltage of −1.20 V. Lee's team reported a Cu–Ni-based RMED smart window using DMSO electrolyte, achieving a maximum optical modulation of 55.2% within a short coloring/bleaching time (6.2 s/13.2 s), but requiring at least −1.50 V for Cu–Zn co-deposition.[22] McGehee's group controlled the morphology and optical properties of the Cu–Bi metal film by using a polymer corrosion inhibitor (polyvinyl alcohol, PVA).[23] Their large-area device, exceeding 900 cm^2, could achieve a 76% optical modulation rate under a voltage drive of −0.80 V. Clearly, Cu (0.31 V) and Bi (0.34 V), with similar standard reduction potentials (*V versus* SHE),[6] present a promising choice for integrated RMEDs powered by solar cells (RMED-SCs) due to their potential for low driving voltage and outstanding optical performance.[24–26]

Inspired by these findings, the objective of the present study is to integrate RMEDs with solar cells to achieve a low-voltage self-powered smart window that can adjust its tint based on dynamic environments while simultaneously harnessing solar energy to improve residential living wellness. Unfortunately, this emerging field has many technologies and scientific mechanisms that remain to be fully explored and understood.[27–31] Therefore, the primary issue that needs to be addressed is how to obtain an electrolyte that benefits from both aqueous and DES solvents *via* an electrolyte additive strategy. Density functional theory (DFT) was utilized to thoroughly understand the interactions between various particles within different electrolyte systems, as well as their interactions with electrodes. COMSOL Multiphysics was employed to simulate the metal electrodeposition and fully comprehend the microscopic mechanisms of additives, particularly the influence of metal ion concentration distribution and current density on the electrodeposition process. Theoretical results indicate that the introduction of choline chloride (ChCl) in water (ChCl + water) is favorable for creating more nucleation sites and lowering the energy barrier for metal ion reduction. Then, the electrodeposition of Cu–Bi in different electrolyte systems was conducted to verify the feasibility of the theoretical predictions. Scanning electron microscopy (SEM), energy-dispersive X-ray spectroscopy (EDX), and Johnson–Mehl–Avrami–Kolmogorov (JMAK) analysis were used to investigate the microscopic reactions and elucidate the function of ChCl in promoting the dense, uniform nucleation and growth of Cu–Bi metal. Elaborate studies on cyclic voltammetry (CV) and electrochemical impedance spectroscopy (EIS) tests were further executed to interpret the effect of ChCl in facilitating the rapid nucleation and growth of metal nanoparticles, thus reducing the driving voltage of RMED. All these attempts aim to reveal Cu–Bi nucleation and growth mechanisms and achieve performance superior to RMEDs with low driving voltages. Furthermore, $Pb(AC)_2$-doped $CsPbI_2Br$ perovskite layers and L-phenylalanine (L-PAA) interface modification layers were proposed to reduce defect state density and achieve a high V_{oc}, ensuring fully reversible metal electrodeposition only under solar illumination. As expected, our RMED-SCs can uniformly switch between a clear state with 82% transmittance and a color-neutral black state possessing 19.58% transmittance, which represents a significantly improved self-powered RMEDs featuring fast switching, color neutrality, and durable cycling features.

2. Experimental section

2.1. Electrolyte solution preparation

5 mM $BiCl_3$, 15 mM $CuCl_2 \cdot 2H_2O$, 1 M LiCl, and 15 mM (2 mM) HCl were dissolved in deionized water to obtain Cu–Bi electrolyte. ChCl and EG were mixed in a mass ratio of 1 : 3 and heated at 50 °C for 30 min to obtain DES. The DES + water solvent was mixed in a volume ratio of 7 : 3 and heated and stirred at 70 °C. The EG in DES + water was replaced by an equal volume of water to obtain a ChCl + water solvent. 10 wt% poly(vinyl alcohol) was dissolved in the Cu–Bi electrolytes to obtain gel electrolytes. SnO_2 was dissolved in deionized water in a volume ratio of 1 : 5 and stirred for 2 h to obtain the SnO_2 solution. 0.5 mg of L-PAA was dissolved in 1 mL of deionized water to obtain the L-PAA solution. CsI (1.2 mol L^{-1}), PbI_2 (0.6 mol L^{-1}), and $PbBr_2$ (0.6 mol L^{-1}) were dissolved in DMSO and stirred at 60 °C for 2 h to obtain the $CsPbI_2Br$ precursor solution. $Pb(Ac)_2 \cdot 3H_2O$ (0.06 mol L^{-1}) was added to the $CsPbI_2Br$ precursor solution (DMSO : DMF = 1 : 5 volume ratio) to obtain the $Pb(Ac)_2$–$CsPbI_2Br$ precursor solution. 72.5 mg of Spiro-OMeTAD was dissolved in 1 mL of CB with 17.5 μL of Li-TFSI (520 mg mL^{-1} in acetonitrile) solution and 28.8 μL of TBP to obtain the Spiro-OMeTAD solution.

2.2. Device fabrication

For RMEDs, the ITO conductive glass was washed twice, first by sonication in water containing detergent, then in tap water, deionized water, and ethanol for 15 min each time. The ITO

10050 | *J. Mater. Chem. A*, 2025, **13**, 10049–10059

This journal is © The Royal Society of Chemistry 2025

glass served as a working electrode. Cu foil was cut into a frame, pasted on a glass sheet, and used as a counter electrode. The RMED was constructed by sandwiching a gel electrolyte between the ITO working electrode and the Cu frame counter electrode while maintaining an interelectrode distance of 2 mm using commercial tape as a spacer.

For perovskite solar cells, the washed ITO conductive glass was dried with nitrogen and then treated with ultraviolet ozone (UVO) for 15 min. The SnO_2 solution was spin-coated onto the ITO substrate at 2500 rpm for 30 s and then annealed at 150 °C for 30 min to obtain the SnO_2 layer. After cooling to room temperature, a thin layer of L-PAA film was spin-coated at 4000 rpm for 30 s and annealed at 125 °C for 10 min. The perovskite precursor solution was spin-coated onto the SnO_2/L-PAA layer at 500 rpm for 5 s and 2500 rpm for 30 s. The perovskite without $Pb(Ac)_2 \cdot 3H_2O$ was heated to 42 °C for 1.5 min and then 160 °C for 10 min, while the perovskite with $Pb(Ac)_2 \cdot 3H_2O$ was heated to 45 °C for 1 min and 250 °C for 10 min. Next, the hole transport layer was deposited on the perovskite layer by spin-coating the Spiro-OMeTAD solution at 3000 rpm for 30 s. Finally, 10 nm of MoO_3 and 100 nm of Ag were subsequently deposited by vacuum thermal evaporation under a pressure of 1×10^{-5} Pa. The active area of each device is ~4 mm^2.

For the RMED-SCs, the substrate area is 15×30 mm^2, with ITO on the left half for preparing solar cells and Cu foil attached to the right half of the glass as the counter electrode for RMED. Commercial tape is used to separate the 15×15 mm^2 ITO glass working electrode from the counter electrode. Wires and metal clips were used to connect the electrodes of the solar cell and RMED.

3. Results and discussion

To reduce the driving voltage of the Cu–Bi system *via* electrolyte optimization and achieve integrated RMED-SCs, an extensive study on the electrolyte was performed. We found that the ethylene glycol (EG) in DES can adsorb on the electrode and occupy the active sites for reduction, which inhibits hydrogen evolution and reduces the reduction of metal ions, thereby lowering the charge transfer constant and the current density. Conversely, the choline cation in ChCl of DES can readily adsorb on the surface of the electrode, inhibiting dendrite generation and growth and inducing more uniform metal deposition. The hydroxyl group in ChCl disrupts the initial hydrogen bond network of the water in the electrolyte, reducing water activity, alleviating side reactions initiated by water, and suppressing hydrogen evolution. Therefore, we introduced ChCl into water to create an innovative Cu–Bi electrolyte with a ChCl + water solvent system, which retains the advantages of both DES and water, namely a high ionic ionization degree, while enabling metal electrodeposition under high current density.

3.1. Electrolyte additive strategy for uniform and dense nucleation of Cu–Bi

Fig. 1a shows the interactions between In_2O_3 with the choline cation (Ch^+), Cu^{2+}, Bi^{3+}, or their corresponding metal complexes

based on DFT calculation. The binding energies for the Ch^+–Bi^{3+} and Ch^+–Cu^{2+} systems with In_2O_3 are −12.63 and −11.72 eV, respectively, which are significantly higher than those of only Bi^{3+} or only Cu^{2+} with In_2O_3 (−10.91 and −7.96 eV), indicating that ChCl promotes the binding of metal ions to the ITO substrate. It is also noted that the binding energies of the Ch^+–$[BiCl_6]^{3-}$ and Ch^+–$[CuCl_4]^{2-}$ systems with In_2O_3 are −13.14 and −12.01 eV, respectively, demonstrating that Ch^+ is beneficial for the reduction of metal ions on the ITO surface by
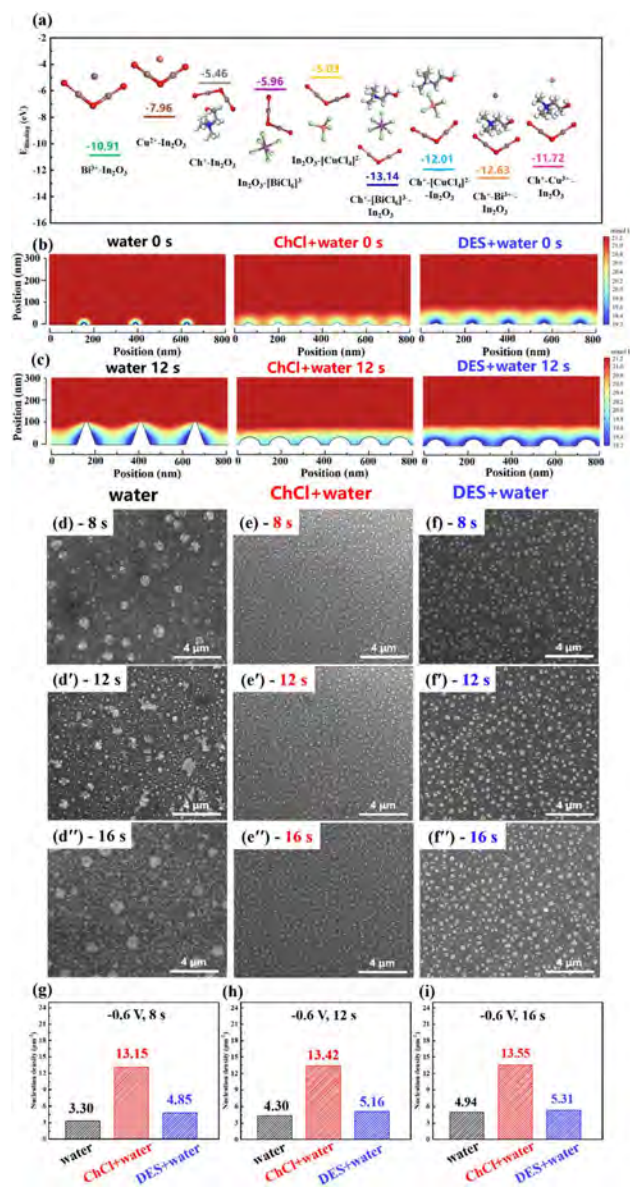

Fig. 1 (a) The binding energies between different ingredients were obtained from DFT calculations. Metal ion concentration distributions at −0.60 V for (b) 0 s and (c) 12 s in water, ChCl + water, and DES + water electrolytes. The SEM images of electrodeposition in the water-based electrolyte under −0.60 V for (d) 8 s, (d′) 12 s, and (d″) 16 s, ChCl + water electrolyte under −0.60 V for (e) 8 s, (e′) 12 s, and (e″) 16 s, DES + water electrolyte under −0.60 V for (f) 8 s, (f′) 12 s, and (f″) 16 s. The corresponding nucleation densities of three electrolytes under deposition times of (g) 8 s, (h) 12 s, and (i) 16 s.

This journal is © The Royal Society of Chemistry 2025

J. Mater. Chem. A, 2025, **13**, 10049–10059 | **10051**

complexation. Hence, our ChCl + water is an ideal choice for the solvent of Cu–Bi metal electrodeposition.

Fig. 1b, c, S1a and b† display the distribution of metal ion concentration and current density at the interface under deposition conditions of −0.60 V for 0 s and 12 s, respectively. Results show that Cu and Bi metals have a relatively sparse nucleation distribution on the substrate in the water electrolyte, prompting preferential deposition at the tip and resulting in uneven distributions of ion concentration and current density. The ChCl + water electrolyte facilitates uniform and dense nucleation and effectively regulates the distribution of metal ion concentration and current density at the interface. The uniformity of metal ion concentration and current density distribution at the interface in the DES + water electrolyte is intermediate compared to the other two samples mentioned above. The simulation results demonstrate that optimizing the ChCl + water electrolyte is favorable for the distribution of metal ion concentration and current density, thus facilitating the formation of a uniform, dense, and dendrite-free Cu–Bi metal film.

To visually present Cu–Bi nucleation and growth during the electrodeposition process, the morphology of particles was analyzed using SEM. Fig. 1d–f, d′–f′ and d″–f″ illustrates SEM images of particles in water-only, ChCl + water, and DES + water at a bias of −0.60 V with 8, 12, and 16 s electrodeposition times. Evidently, the Cu–Bi particles deposited in the water-only electrolyte are relatively sparse, irregular, and exhibit uneven size distribution. In comparison, particles in ChCl + water have the most uniform size distribution, followed by those in DES + water electrolytes. The same trend can also be observed at the deposition voltage of −0.7 V (Fig. S2†).

The nucleation density, average particle size, and surface coverage ratio of three electrolytes at −0.60 V and −0.70 V for 8, 12, and 16 s deposition conditions are quantified in Table 1 and S1.† At −0.60 V for 16 s, the nucleation density of ChCl + water reaches up to 13.55 μm^{-2}, which is much higher than that of water (4.94 μm^{-2}) and DES + water (5.31 μm^{-2}), and the nucleation densities in all three electrolytes do not change significantly as the deposition time changes. Accordingly, the ChCl + water electrolyte also possesses the highest surface coverage ratio of 44.83% (Fig. S3a†). Fig. 1g–i shows their corresponding nucleation density histogram. Our results confirm that the nucleation density obtained from the ChCl + water electrolyte is the highest under the same bias and deposition

time among the three electrolytes. A higher nucleation density and narrower particle size distribution are conducive to forming a denser metal film. Furthermore, a higher applied negative bias or longer deposition time results in higher nucleation density, average particle size, and surface coverage ratio, regardless of the electrolyte type.

The JMAK analysis elaborated in Fig. 2 was applied to gain an in-depth understanding of the metal nucleation/growth kinetics during the electrodeposition process. Each cycle of the JMAK test included 0 V for 2 s and −1 V for 10 s. There was a current surge stage, followed by a current saturation stage in all the cycles, which corresponded to the nucleation and growth of metal particles, respectively.[32,33] The curves of time *versus* normalized current for the ChCl + water electrolyte are demonstrated in Fig. 2a and b. The double logarithmic graphs of $-\ln(1 − X)$ and t were obtained (Fig. 2c and d). Fig. S3b–i† show the JMAK measurements for water-only and DES + water electrolytes. The values of the crystal growth geometry factor n in Fig. 2e exhibit an upward trend and approach 3 as the cycle period increases, indicating that crystal nuclei growth in the later stages tends to be three-dimensional. In contrast, the crystal nucleation frequency k values pass through a maximum in Fig. 2f. The initial increase in k can be attributed to the large number of nucleation sites on the ITO surface, while the subsequent decrease is caused by the reduction of available nucleation sites. Initially, abundant Cu–Bi nanoparticles grow on the ITO surface, occupying nearly all nucleation sites. Subsequent metal deposition primarily occurs on the already nucleated particles, and the nucleation behavior gradually shifts from forming new nuclei to growing existing particles. Overall, during the 2000 cycles, the k value for electrodeposition with the ChCl + water electrolyte is higher than that for water and DES + water electrolytes.

EDX was applied to investigate the distribution of Cu–Bi particles. Fig. 3a–c shows the elemental ratios under the deposition conditions of −0.60 V for 8 s. It is evident that the proportion of Cu in the ChCl + water electrolyte is the highest. Similar trends are observed in Fig. S4–S6,† which present the EDX images of Cu–Bi particles deposited at −0.60 and −0.70 V for 8, 12, and 16 s in water, ChCl + water, and DES + water electrolytes. The elemental distribution ratios under all the above deposition conditions are listed in Table S2.† Moreover, the proportion of Cu in the same electrolyte solution and under varying deposition bias voltages consistently increases with

Table 1 The nucleation densities, average particle sizes, and surface coverage ratios at −0.60 V for 8, 12, and 16 s

| Deposition conditions	Evaluation parameter	Water	ChCl + water	DES + water
−0.60 V, 8 s	Nucleation density (μm^{-2})	3.30	13.15	4.85
	Average particle size (nm)	70.65	57.63	68.47
	Surface coverage ratio (%)	17.02	30.88	17.43
−0.60 V, 12 s	Nucleation density (μm^{-2})	4.30	13.42	5.16
	Average particle size (nm)	72.93	67.64	70.80
	Surface coverage ratio (%)	25.62	35.51	26.84
−0.60 V, 16 s	Nucleation density (μm^{-2})	4.94	13.55	5.31
	Average particle size (nm)	76.59	73.78	74.29
	Surface coverage ratio (%)	32.57	39.63	33.69
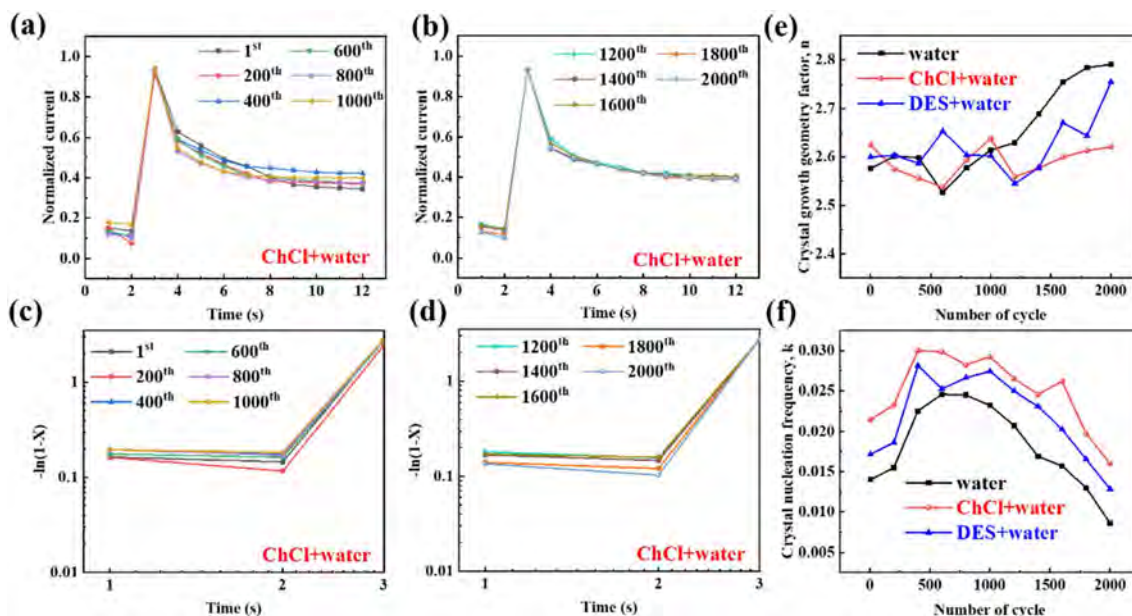
Fig. 2   The normalized current–time curves of electrodeposition with ChCl + water electrolyte under different cycling times: (a) 1st to 1000th cycles and (b) 1200th to 2000th cycles. The double logarithmic plots of −ln(1 − X) *versus t* under different cycling numbers: (c) 1st to 1000th cycles and (d) 1200th to 2000th cycles. The crystal growth geometry factor *n* (e) and the crystal nucleation frequency *k* (f) during the deposition process of three different electrolytes.

longer deposition times. This behavior is observed in all three electrolyte solutions, attributed to the mechanism based on the galvanic displacement of Bi by Cu^+. In three Cu–Bi electrolyte solutions, ChCl + water facilitates the formation of spherical Cu particles because the electrochemically reductive Cu^+ oxidizes the deposition of dendritic Bi into spherical particles (eqn (1)).[34] The displacement reaction occurs simultaneously with the electrochemical reduction of Bi^{3+} and Cu^{2+}/Cu^+ to Bi and Cu, as mentioned previously. To sum up, EDX results reveal that ChCl + water significantly contributes to forming more uniform and

denser Cu–Bi particles, which aligns well with the SEM results in Fig. 1.

$$3Cu^+ + Bi \rightarrow Bi^{3+} + 3Cu \qquad (1)$$

3.2   Mechanism of electrochemical nucleation on low-voltage-driven RMEDs

Further experiments on Cu–Bi electrodeposition with four different solvents (water, DES + water, ChCl + water, and DES)
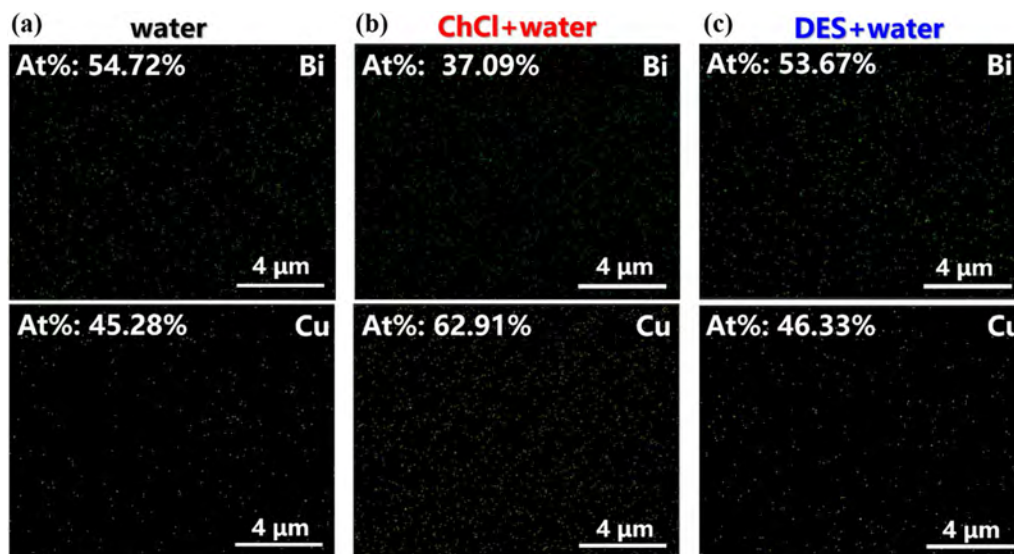

Fig. 3   The EDX diagrams of Bi and Cu elements under the deposition condition of −0.60 V for 8 s, when the solvents are (a) water, (b) ChCl + water, and (c) DES + water.

This journal is © The Royal Society of Chemistry 2025

J. Mater. Chem. A, 2025, **13**, 10049–10059 | **10053**

were conducted to verify the theoretical predictions. Cu–Bi electrolytes with a high concentration of Bi^{3+} deposit insoluble dendritic Bi, which reduces surface coverage ratio and optical contrast, while a high concentration of Cu^{2+} produces CuBr precipitation. A Cu^{2+} : Bi^{3+} ratio of 15 mM to 5 mM has proven to be optimal. Fig. 4a shows cyclic voltammetry (CV) curves of Cu–Bi electrolytes to study the electrochemical reaction process during cycling. Using the ChCl + water electrolyte as an example, during the negative scanning process, the three reduction peaks correspond sequentially to the reduction of Cu^{2+} to Cu^+, Bi^{3+} to Bi, and Cu^+ to Cu. In the subsequent forward sweep, the anodic current begins to increase at -0.23 V, corresponding to the dissolution of deposited Cu and Bi back to Cu^+ and Bi^{3+}. Later, the second anodic peak represents the oxidation of Cu^+ to Cu^{2+}.[35] According to the CV curves, the ChCl + water electrolyte exhibits distinct redox peaks and the highest current density (12.46 mA cm^{-2} at 0.052 V).

The DES-only (a mixture of ChCl and EG) displays almost no reduction peak and displays an extremely low current density (2.79 mA cm^{-2} at -0.063 V) due to EG's restraining effects. The current densities of DES + water and water-only electrolytes are also lower than that of ChCl + water. Compared to the water-only electrolyte, there is a slight negative shift in reduction potential for both DES + water and ChCl + water electrolytes. This may be attributed to the tendency of both ChCl and EG to adsorb on the electrode surface, exerting an inhibitory effect on the reduction reaction.[36] While Cu and Bi metal deposition occurs on the working electrode, Cl^- is oxidized to ClO^- on the counter electrode to balance the reduction reaction on the working electrode.

The solubility of Bi greatly relies on the acid concentration, as Bi is a strong Lewis acid in the Cu–Bi electrolyte. To prevent the formation of insoluble precipitates, typically 15 mM hydrochloric acid (HCl) is added to the Cu–Bi electrolyte. However, high concentrations of up to 15 mM HCl can corrode ITO and decrease the cyclic durability of devices.[37] Meanwhile, passivation effects in aqueous electrolytes can induce insoluble oxides or hydroxides on the electrode surface, which may hinder the corrosion effects of HCl. Therefore, a trade-off between the passivation and corrosion effects is evaluated, and 2 mM HCl is added to the ChCl + water and DES + water electrolytes in the following study. Results indicate no significant difference in the CV curves of the ChCl + water electrolyte (Fig. S7a†), whether the amount of HCl is 2 mM or 15 mM. However, a significant reduction in current density is observed when the amount of HCl is reduced to 2 mM in the DES + water electrolyte (Fig. S7b†). Comparatively, the current density of DES + water electrolyte is much lower than that of ChCl + water electrolyte with 2 mM HCl (Fig. S7c†).

Fig. 4b and S7d–e† show CV curves at different scan rates in ChCl + water, DES + water, and water-only electrolytes, respectively. When the scan rates are set to 20–100 mV s^{-1}, although there is a slight shift in the redox peaks, the shapes of the curves remain almost unchanged. The electrochemical kinetic behaviors of electrolytes are compared based on the peak current density at different scan rates and its relationship with the square root of the scan rate (Fig. 4c). According to the Randles–

Sevcik equation (eqn S3†), a higher linear slope indicates a higher diffusion coefficient,[38] reflecting the level of ionic conductivity (eqn S4†). The slope of the ChCl + water curve (1.11) is significantly larger than that of the DES + water (0.61) and water (0.46) curves, suggesting that the ChCl + water electrolyte has higher diffusion coefficients and ionic conductivity.

To further understand the ion transport behavior in different electrolytes, electrochemical impedance spectroscopy (EIS) was measured (Fig. 4d and S7f†). The charge transfer resistance R_{ct} of the ChCl + water electrolyte is 647 Ω cm^2, much lower than that of DES + water (2217 Ω cm^2), water (3834 Ω cm^2), and DES-based (11176 Ω cm^2) electrolytes (Table 2), demonstrating more effective ion transport. Further calculations of ionic conductivities in each electrolyte were explored, resulting in values of 0.05, 0.31, and 0.09 S m^{-1}, respectively. The diffusion coefficients of Cu^{2+} and Bi^{3+} during the reduction process can be obtained based on eqn S5†.[39] Similarly, the ChCl + water electrolyte shows the highest diffusion coefficients of 7.84×10^{-6} (Cu^{2+}) and 2.04×10^{-5} cm^2 s^{-1} (Bi^{3+}) as shown in Fig. 4e. These values are consistent with the results of Fig. 4c, indicating that the reduction reactions proceed more easily in ChCl + water, facilitating a lower driving voltage.

Fig. 4f shows the change in optical density (ΔOD) *versus* injected charge per unit area (ΔQ) during electrodeposition, with the corresponding coloration efficiency (CE) values[40] being 10.41 (ChCl + water), 8.36 (DES + water), and 8.17 (water-only) cm^2 C^{-1}, respectively. Chronoamperometry (CA) was conducted to evaluate the stability and reversibility of the ChCl + water electrolyte (Fig. 4g). The current density remains stable by applying voltages of +1.00 V *vs.* Ag/AgCl and -1.00 V *vs.* Ag/AgCl for 1000 repeated cycles. Multiple CV scans also confirm that the cycling stability of the ChCl + water electrolyte has been significantly improved compared to that of the water-only electrolyte (Fig. S8†). These results support the claim that ChCl promotes the rapid, dense, and uniform nucleation of Cu–Bi metal particles at a low driving voltage.

Further tests of RMEDs need to be conducted to draw further conclusions. Hence, 10 wt% poly(vinyl alcohol) was dissolved in Cu–Bi electrolytes to obtain gel electrolytes for further fabricating sandwich-structured RMEDs. Fig. 4h–j, h′–j′ and h″–j″ demonstrate photographs of water-only-, ChCl + water-, and DES + water-based RMEDs operated at different driving voltages. As can be seen, the colors of all RMEDs gradually darken as the voltage increases from 0 to -0.58 and -0.60 V. For the ChCl + water device, the transmittance at 400 nm decreases to 27.96% at -0.60 V for 2 min, down from an initial 45.23% at -0.58 V for 2 min, which is significantly lower than that of the water-only (from 58.38% to 46.79%) and DES + water (from 62.85% to 49.73%).

The maximum transmittance difference at a given wavelength is defined as the device's optical modulation (ΔT),[29] an important parameter for evaluating the optical performance of RMEDs. The ΔT of the ChCl + water device at 800 nm is 47.78%, significantly higher than that of water-only (31.24%) and DES + water (30.04%) devices (Fig. 4k–m). In addition, the lowest transmittance fluctuation factor (T_{ff}) was found in the ChCl + water device at -0.58 and -0.60 V (eqn S6 and Table S3†),
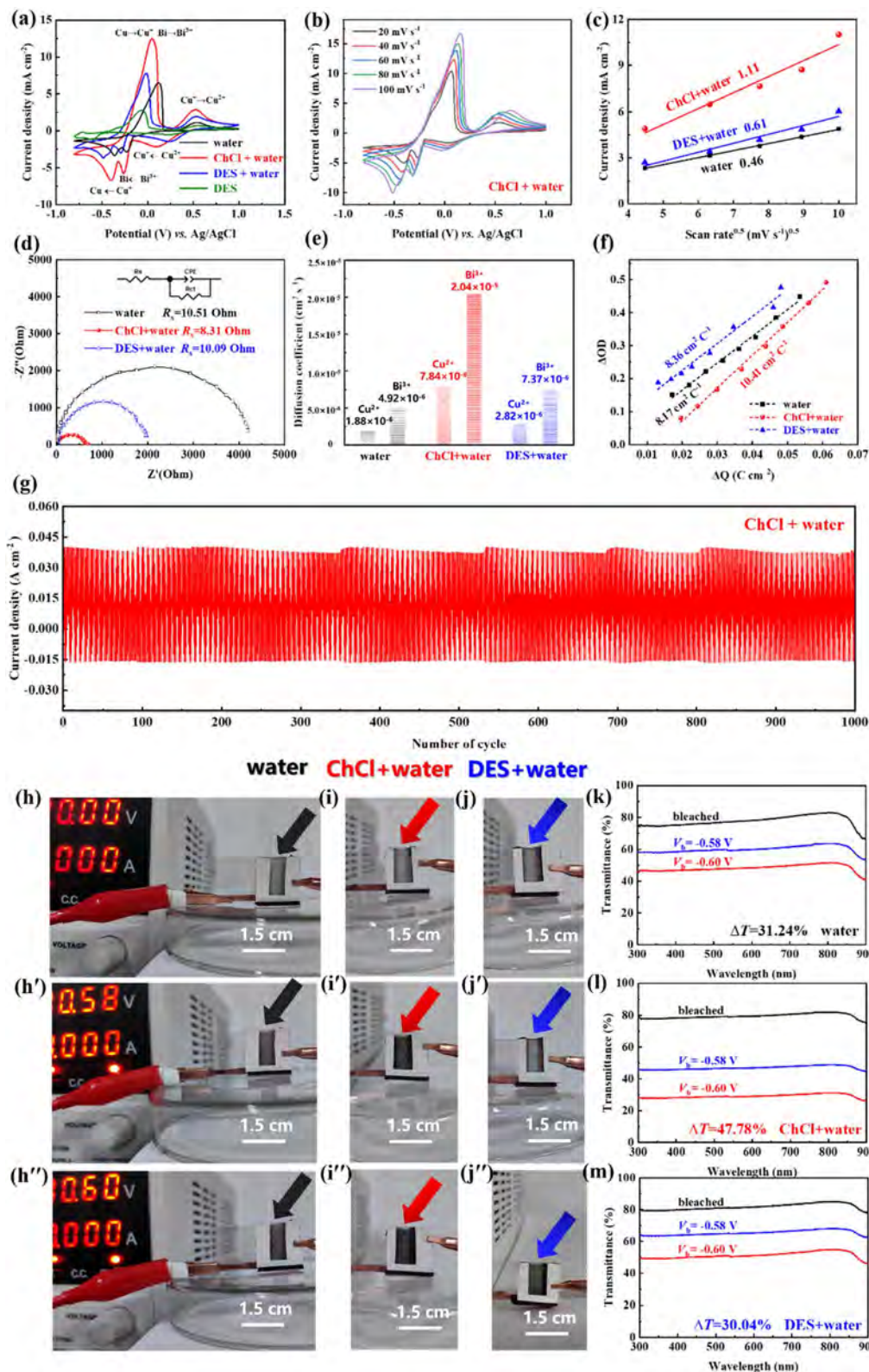
Fig. 4 (a) CV curves of four electrolytes. (b) CV curves of ChCl + water electrolyte at different scanning rates. (c) Corresponding peak current function of the square root of the scanning rates, (d) EIS plots, (e) diffusion coefficients of Cu^{2+} and Bi^{3+}, and (f) curves of optical density and injected charge density based on water, ChCl + water, and DES + water electrolytes. (g) Chronoamperometry cycle stability of electrodeposition in ChCl + water electrolyte. RMEDs fabricated with (h–h″) water, (i–i″) ChCl + water, and (j–j″) DES + water electrolyte at driving voltages of 0, −0.58, and −0.60 V. Transmittance of RMEDs with (k) water, (l) ChCl + water, and (m) DES + water electrolytes at driving voltages of 0, −0.58, and −0.60 V.

This journal is © The Royal Society of Chemistry 2025

J. Mater. Chem. A, 2025, 13, 10049–10059 | 10055

Table 2 The EIS fitting parameters of four different electrolytes

EIS parameters	ChCl + water	DES + water	Water	DES
R_s (Ω cm^2)	8.31	10.09	10.51	18.31
CPE-T	1.71×10^{-5}	8.83×10^{-6}	1.21×10^{-5}	6.52×10^{-6}
CPE-P	0.92	0.88	0.69	0.63
R_{ct} (Ω cm^2)	647	2217	3834	11176

indicating better neutral coloration during electrodeposition. In summary, the ChCl + water RMED exhibits the largest optical contrast and neutral color, which is beneficial for constructing dynamic color-changing windows with low self-driven voltage.

3.3 CsPbI$_2$Br solar cells facilitate low-voltage self-powered dynamic windows

Another important issue is obtaining a power supply with high working voltage for a desirable self-powered dynamic window. To improve the V_{oc} of solar cells, a Pb(AC)$_2$-doped CsPbI$_2$Br perovskite layer and L-PAA interface modification layer are proposed to reduce defect state density. Fig. 5a shows the architecture of CsPbI$_2$Br solar cells, in which a 40 nm L-PAA was adopted to passivate SnO$_2$ and perovskite layers. The SnO$_2$/CsPbI$_2$Br, SnO$_2$/Pb(Ac)$_2$-CsPbI$_2$Br, and SnO$_2$/L-PAA/CsPbI$_2$Br control devices were also prepared, with current density–voltage (J–V) and external quantum efficiency (EQE) curves presented in Fig. 5b and c.
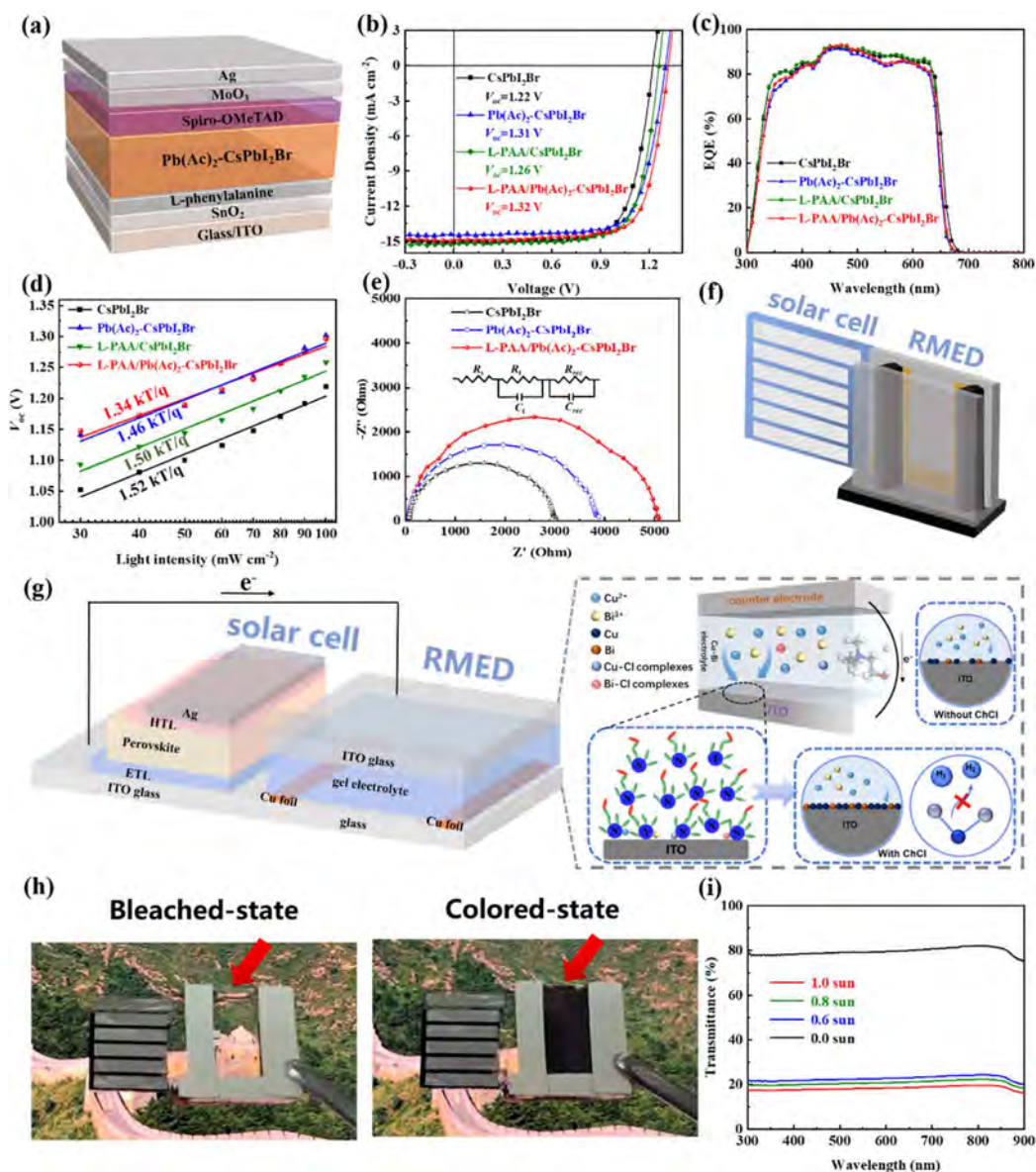

Fig. 5 (a) Device structure, (b) J–V curves, (c) EQE curves, (d) V_{oc} light intensity dependence test, and (e) electrochemical impedance Nyquist plots of the solar cells. (f) A schematic diagram of the RMED-SCs. (g) A schematic diagram of the electrodeposition mechanism in the ChCl + water solvent system. (h) Photographs of the RMED-SCs under bleached and colored state. (i) Transmission of the RMED-SCs illuminated by sunlight intensities from 0.60 to 1.00 sun.

Both SnO$_2$ and SnO$_2$/L-PAA demonstrate excellent optical transmittance and low absorption (Fig. S9a†), ensuring efficient light absorption by the perovskite layer, further confirmed by the absorption spectra of perovskite films grown on SnO$_2$ and SnO$_2$/L-PAA electron transport layers (ETLs) (Fig. S9b†). The Tauc plot of the SnO$_2$/L-PAA film, calculated from the UV-vis absorption spectra, is shown in the inset of Fig. S9a,† indicating a bandgap of 3.76 eV. The conductivities (σ) of SnO$_2$/L-PAA and SnO$_2$ films are 3.416×10^{-3} and 2.658×10^{-3} mS cm^{-1} (Fig. S9c†), which were measured with a device of ITO/ETL/Au (eqn S7†).[41]

For photovoltaic performances (Table 3), significant enhancements of V_{oc} are observed after introducing the L-PAA interface layer (from 1.22 to 1.26 V) and Pb(Ac)$_2$ doping (from 1.22 to 1.31 V) compared to the CsPbI$_2$Br device. The device modified with an L-PAA interface layer and doped with Pb(Ac)$_2$ achieves a champion V_{oc} of 1.32 V, a fill factor (FF) of 74.07%, and a power conversion efficiency (PCE) of 14.47%. Moreover, the L-PAA/Pb(Ac)$_2$-CsPbI$_2$Br device possesses the lowest series resistance ($R_s' = 8.19$ Ω cm^2) and the highest shunt resistance ($R_{sh}' = 1136$ Ω cm^2). The enhancement of V_{oc} can be attributed to the partial replacement of the I$^-$ replaced by the acetate anion (Ac$^-$) in CsPbI$_2$Br, which reduces the defect state density of the perovskite film and increases carrier lifetime.[42,43] The L-PAA, with electron-rich units of –COOH, can interact with uncoordinated Pb^{2+} and Sn^{2+}. The lone pair electrons of N atoms in –NH$_2$ can be transferred to the perovskite layer to compensate for acceptors, effectively passivating interface defects and preventing charge accumulation, thereby accelerating charge transfer.[44,45] As a result, bidirectional passivation suppresses non-radiative recombination, resulting in a higher expected V_{oc}.

Fig. S9d† displays the ultraviolet photoelectron spectroscopy (UPS) diagram of SnO$_2$/L-PAA, while Fig. S9e and f† presents the secondary electron cutoff diagram and onset diagram[46] of SnO$_2$/L-PAA, respectively. The work function, highest occupied molecular orbital (HOMO), and lowest unoccupied molecular orbital (LUMO) levels of SnO$_2$/L-PAA are −4.41, −7.99 and −4.23 eV, respectively. The schematic energy levels of the materials involved in this work are shown in Fig. S9g.†[47]

The light intensity-dependent V_{oc} was tested to analyze the recombination mechanism under light intensities of 30–100 mW cm^{-2} (Fig. 5d). The slopes of V_{oc} against the logarithm of light intensity for the Pb(Ac)$_2$-CsPbI$_2$Br and L-PAA/CsPbI$_2$Br devices (1.46 $k_B T/q$ and 1.50 $k_B T/q$) are both smaller than that of the CsPbI$_2$Br device (1.52 $k_B T/q$), indicating that both L-PAA and Pb(Ac)$_2$ are effective in reducing trap-assisted recombination.

The slope of the L-PAA/Pb(Ac)$_2$-CsPbI$_2$Br device (1.34 $k_B T/q$) is the lowest, demonstrating a significant suppression of the trap-assisted recombination process within the device.[48]

EIS tests were conducted to understand the enhancement of electrical properties in the devices, as shown in Fig. 5e (the inset plots the equivalent circuit). Table S4† indicates the EIS fitting parameters. The recombination resistance R_{rec} of the L-PAA/Pb(Ac)$_2$-CsPbI$_2$Br devices is 4690 Ω cm^2, significantly higher than that of the CsPbI$_2$Br (2921 Ω cm^2) and Pb(Ac)$_2$-CsPbI$_2$Br (3770 Ω cm^2) devices. A higher R_{rec} indicates reduced recombination.[49] Notably, the charge transfer resistance R_t of the L-PAA/Pb(Ac)$_2$-CsPbI$_2$Br device is 309.14 Ω cm^2, which is smaller than that of the CsPbI$_2$Br (809.51 Ω cm^2) and Pb(Ac)$_2$-CsPbI$_2$Br (686.27 Ω cm^2) devices. These results demonstrate that Pb(Ac)$_2$ and L-PAA enhance charge transport performance, thereby achieving a high V_{oc}.

Based on these efforts, integrated RMED-SCs were designed (Fig. 5f), and the corresponding equivalent circuit model is shown in Fig. S9h.† The device's microcosmic mechanism is illustrated in Fig. 5g, where ChCl adsorbs on the ITO electrode to form more nucleation sites while simultaneously reducing the energy barrier for the reduction of Cu^{2+} and Bi^{3+} to Cu and Bi. The Cl$^-$ in Cu–Bi electrolyte forms a small amount of complexes with metal ions, such as [BiCl$_6$]$^{3-}$ and [CuCl$_4$]$^{2-}$. The Ch$^+$ adsorbed on the ITO also provides corresponding nucleation sites,[50] leading to the uniform deposition of dense nanoparticles under lower bias. The hydroxyl group in ChCl disrupts the initial hydrogen bond network of water in the electrolyte, reduces water activity, alleviates side reactions initiated by water, and suppresses hydrogen evolution.[51]

The output voltage of the solar cell (under sunlight illumination) successfully induces optical tinting of the RMED-SCs (ChCl + water-based). Photographs of RMED-SCs in a transparent state without bias and a black state powered by solar cells are shown in Fig. 5h. To further characterize the optical performance of the integrated device, Fig. 5i displays the transmittance spectra with sunlight intensity from 0.60 to 1.00-sun and without sunlight illumination. Devices without illumination maintain flat transmittance spectra in the visible and near-infrared regions (NIR), ideal for achieving a neutral color. Under 100 mW cm^{-2} sunlight intensity, the transmittance of the RMED-SC at 800 nm decreases from 82.00% (no bias) to 19.58% (powered by solar cells). Even at 0.60 sunlight intensity (60 mW cm^{-2}), the transmittance of RMED-SC at 800 nm is reduced to 24.22%. Thus our RMED-SC achieves significant optical modulation through self-powered operation under sunlight illumination, showcasing important application

Table 3 Photovoltaic performance parameters for solar cells with different active layers and ETLs under the illumination of AM 1.5 G, 100 mW cm^{-2}

Samples	J_{sc} (mA cm^{-2})	V_{oc} (V)	FF (%)	PCE (%)	EQE (mA cm^{-2})	R_s' (Ω cm^2)	R_{sh}' (Ω cm^2)
CsPbI$_2$Br	15.07	1.22	72.85	13.39	14.83	9.79	917
Pb(Ac)$_2$-CsPbI$_2$Br	14.47	1.31	71.10	13.46	14.07	8.78	1064
L-PAA/CsPbI$_2$Br	15.13	1.26	73.01	13.59	14.90	9.05	1031
L-PAA/Pb(Ac)$_2$-CsPbI$_2$Br	14.83	1.32	74.07	14.47	14.34	8.19	1136

potential in modern energy-saving buildings, even in low-light conditions or cloudy days.

4. Conclusion

An electrolyte additive strategy is proposed to facilitate efficient Cu–Bi electrodeposition and achieve RMED-SCs with low self-driving voltage, combining RMED and CsPbI$_2$Br solar cells. Our studies indicate that ChCl not only reduces the energy barrier for converting Cu^{2+} and Bi^{3+} to Cu and Bi but also provides more nucleation sites, resulting in a higher optical contrast of 47.78% at a bias of -0.60 V, in addition to improving CE from 8.17 to 10.41 cm^2 C^{-1}. Nucleation mechanism analysis, conducted using JMAK and EDX, reveals that ChCl + water electrolyte favorably increases nucleation frequency and supports high diffusion coefficients of Bi^{3+} (2.04×10^{-5} cm^2 s^{-1}) and Cu^{2+} (7.84×10^{-6} cm^2 s^{-1}). These results clearly demonstrate that the introduction of ChCl enables fast, uniform, and dense Cu–Bi metal electrodeposition, thereby reducing drive voltage. Moreover, the introduction of the L-PAA interface modification layer and the strategy of Pb(Ac)$_2$ doping in CsPbI$_2$Br achieves a high V_{oc} of up to 1.32 V, guaranteeing complete Cu–Bi deposition even when solar illumination decreases to 0.60-sun. With the synergetic effects of electrolyte and voltage enhancement, an RMED-SC with 62.42% optical contrast has been realized. Therefore, it is reasonable to conclude that low-voltage self-powered dynamic windows hold great application potential in photovoltaic building integration.

Conflicts of interest

The authors declare that they have no known competing financial interests or personal relationships that could have appeared to influence the work reported in this paper.

Acknowledgements

References

1 C. Su, Z. Zhao, D. He, H. Song, C. Zhao and W. Mai, *Nano Energy*, 2023, **111**, 108396.

2 *View dynamic glass, Study: natural light is the best medicine for the office*, https://www.prnewswire.com/news-releases/study-natural-light-is-the-best-medicine-for-the-office-300590905.html, 2018.

3 J. Wang, Y. Lv, Y. Zhou, S. Jia, F. Zhu, O. G. Schmidt and G. Cai, *APL Energy*, 2024, **2**, 011501.

4 S. Qiu, Y. Zhao, K. Wang, J. Luo, R. Wang, X. Jiang, J. Chen, A. Y. Elezzabi, W. Zhang, H. Jia and H. Li, *Mater. Rep.: Energy*, 2024, **4**, 100293.

5 H. Ling, J. Wu, F. Su, Y. Tian and Y. J. Liu, *Nat. Commun.*, 2021, **12**, 1010.

6 C. J. Barile, D. J. Slotcavage, J. Hou, M. T. Strand, T. S. Hernandez and M. D. McGehee, *Joule*, 2017, **1**, 133–145.

7 Y. Zhao, Q. Liu, Y. Wang, H. Liu, M. Lv, P. Cheng, Y. Fu, J. Li and D. He, *Cell Rep. Phys. Sci.*, 2022, **3**, 101100.

8 J. Tian, K. Zhang, Z. Xie, Z. Peng, J. Zhang, A. Osvet, L. Luer, T. Kirchartz, U. Rau, N. Li and C. J. Brabec, *ACS Energy Lett.*, 2022, **7**, 4071–4080.

9 L. Song, *Mater. Rep.: Energy*, 2022, **2**, 100171.

10 Z. Jia, Y. Sui, L. Qian, X. Ren, Y. Zhao, R. Yao, L. Wang, D. Chao and C. Yang, *Nat. Commun.*, 2024, **15**, 6110.

11 G. Liang, F. Mo, H. Li, Z. Tang, Z. Liu, D. Wang, Q. Yang, L. Ma and C. Zhi, *Adv. Energy Mater.*, 2019, **9**, 1901838.

12 J. Chen, A. Naveed, Y. Nuli, J. Yang and J. Wang, *Energy Storage Mater.*, 2020, **31**, 382–400.

13 M. Schlesinger and M. Paunovic, *Modern Electroplating*, John Wiley & Sons, 2011.

14 X. Tao, D. Liu, J. Yu and H. Cheng, *Adv. Opt. Mater.*, 2021, **9**, 2001847.

15 Z. Jia, Y. Su, L. Qian, X. Ren, Y. Zhao, R. Yao, L. Wang, D. Chao and C. Yang, *Nat. Commun.*, 2024, **15**, 6110.

16 G. R. McAndrews, A. L. Yeang, Y. Cai, C. J. Barile and M. D. McGehee, *Adv. Energy Mater.*, 2023, **13**, 2202843.

17 B. B. Hansen, S. Spittle, B. Chen, D. Poe, Y. Zhang, J. M. Klein, A. Horton, L. Adhikari, T. Zelovich, B. W. Doherty, B. Gurkan, E. J. Maginn, A. Ragauskas, M. Dadmun, T. A. Zawodzinski, G. A. Baker, M. E. Tuckerman, R. F. Savinell and J. R. Sangoro, *Chem. Rev.*, 2020, **121**, 1232.

18 E. L. Smith, A. P. Abbott and K. S. Ryder, *Chem. Rev.*, 2014, **114**, 11060–11082.

19 A. P. Abbott, G. Capper, D. L. Davies, K. J. McKenzie and S. U. Obi, *Chem. Eng. Data.*, 2006, **51**, 1280–1282.

20 A. L.-S. Eh, J. Chen, X. Zhou, J.-H. Ciou and P. S. Lee, *ACS Energy Lett.*, 2021, **6**, 4328–4335.

21 L. Wang L, X. Jiao, D. Chen and T. Wang, *Adv. Sci.*, 2022, **9**, 2104121.

22 X. Guo, J. Chen, A. L.-S. Eh, W. C. Poh, F. Jiang, F. Jiang, J. Chen and P. S. Lee, *ACS Appl. Mater. Interfaces*, 2022, **14**, 20237–20246.

23 M. T. Strand, T. S. Hernandez, M. G. Danner, A. L. Yeang, N. Jarvey, C. J. Barile and M. D. McGehee, *Nat. Energy*, 2021, **6**, 546–554.

24 S. M. Islam, T. S. Hernandez, M. D. McGehee and C. J. Barile, *Nat. Energy*, 2019, **4**, 223–229.

25 A. L. Yeang, T. S. Hernandez, M. T. Strand, D. J. Slotcavage, E. Abraham, I. I. Smalyukh, C. J. Barile and M. D. McGehee, *Adv. Energy Mater.*, 2022, **12**, 2200854.

10058 | *J. Mater. Chem. A*, 2025, **13**, 10049–10059

This journal is © The Royal Society of Chemistry 2025

26 T. V. Nguyen, H. H. Do, W. Guo, M. Tekalne, Q. V. Le, T. P. Nguyen, J. H. Cho, S. H. Ahn and S. Y. Kim, *Electron. Mater. Lett.*, 2022, **18**, 36–46.

27 C. Li, R. Tao, Y. Ding, C. Liu, X. Ding, H. Xu, C. Zhi, C. Jia and Z. Li, *Sol. RRL*, 2022, **6**, 2101009.

28 M. Batmunkh, Y. L. Zhong and H. Zhao, *Adv. Mater.*, 2020, **32**, 2000631.

29 Y. Bai, S. Tian, Y. Guan, X. Wang, F. Wang, M. Li, Z. Tan and G. Liu, *Small*, 2024, **20**, 2402903.

30 G. H. Lee, C. J. An, H. I. Lee, J. S. Kim, M. S. Jo, T. H. Ha, K. Baek and C. W. Moon, *Electron. Mater. Lett.*, 2024, **20**, 657.

31 X. Zheng, T. Ahmad and W. Chen, *Energy Storage Mater.*, 2021, **39**, 365–394.

32 R. Saeki and T. Ohgai, *Crystals*, 2019, **9**, 142.

33 L. Guo, G. Oskam, A. Radisic, P. M. Hoffmann and P. C. Searson, *J. Phys. D: Appl. Phys.*, 2011, **44**, 443001.

34 T. S. Hernandez, C. J. Barile, M. T. Strand, T. E. Dayrit, D. J. Slotcavage and M. D. McGehee, *ACS Energy Lett.*, 2017, **3**, 104–111.

35 D. He, C. Su, C. Zhao, G. Yan, Z. Zhao and W. Mai, *Chem. Eng. J.*, 2022, **438**, 135469.

36 Y. J. Han, X. Zhang and G. W. Leach, *Langmuir*, 2014, **30**, 3589–3598.

37 J. E. A. M. van den Meerakker, P. C. Baarslag and M. Scholten, *J. Electrochem. Soc.*, 1995, **142**, 2321.

38 H. Zhang, F. Sun, J. Feng, H. Ling, D. Zhou, G. Cao, S. Wang, F. Su, Y. Tian and Y. Tian, *Cell Rep. Phys. Sci.*, 2022, **3**, 101193.

39 C. Su, M. Qiu, Y. An, S. Sun, C. Zhao and W. Mai, *J. Mater. Chem. C*, 2020, **8**, 3010–3016.

40 G. Yang, Y.-M. Zhang, Y. Cai, B. Yang, C. Gu and S. X.-A. Zhang, *Chem. Soc. Rev.*, 2020, **49**, 8687–8720.

41 Q. Geng, X. Jia, Z. He, Y. Hu, Y. Gao, S. Yang, C. Yao and S. Zhang, *Adv. Mater. Interfaces*, 2022, **9**, 2201641.

42 H. Zhao, Y. Han, Z. Xu, C. Duan, S. Yang, S. Yuan, Z. Yang, Z. Liu and S. Liu, *Adv. Energy Mater.*, 2019, **9**, 1902279.

43 W. Shen, Y. Dong, F. Huang, Y. B. Cheng and J. Zhong, *Mater. Rep.: Energy*, 2021, **1**, 100060.

44 B. Hu, J. Zhang, Z. Guo, L. Lu, P. Li, M. Chen and C. Li, *ACS Appl. Mater. Interfaces*, 2022, **14**, 15840–15848.

45 H. Jin, E. Debroye, M. Keshavarz, I. G. Scheblykin, M. B. J. Roeffaers, J. Hofkens and J. A. Steele, *Mater. Horiz.*, 2020, **7**, 397–410.

46 Y. Bai, C. Zhao, X. Chen, S. Zhang, S. Zhang, T. Hayat, A. Alsaedi, Z. Tan, J. Hou and Y. Li, *J. Mater. Chem. A*, 2019, **7**, 15887–15894.

47 Y. Bai, F. Han, R. Zeng, S. Tian, F. Wang, X. Wang, M. Dai, M. Li and Z. Tan, *J. Mater. Chem. A*, 2023, **11**, 17514–17524.

48 S. Jiang, R. Wang, M. Li, R. Yu, F. Wang and Z. Tan, *Energy Environ. Sci.*, 2024, **17**, 219–226.

49 L. Yan, Q. Xue, M. Liu, Z. Zhu, J. Tian, Z. Li, Z. Chen, Z. Chen, H. Yan, H.-L. Yip and Y. Cao, *Adv. Mater.*, 2018, **30**, 1802509.

50 A. H. Whitehead, M. Pölzler and B. Gollas, *J. Electrochem. Soc.*, 2010, **157**, D328.

51 C. Xiao, R. Yao, H. Zhu, L. Qian and C. Yang, *Chem. Commun.*, 2022, **58**, 10088–10090.